2013

Tidally induced lateral dispersion of the Storfjorden overflow plume

Wobus, F

10.5194/os-9-885-2013
Ocean Science
Copernicus GmbH

Ocean Sci., 9, 885–899, 2013
www.ocean-sci.net/9/885/2013/
doi:10.5194/os-9-885-2013

Ocean Science Open Access

Tidally induced lateral dispersion of the Storfjorden overflow plume

F. Wobus[1], **G. I. Shapiro**[1,2], **J. M. Huthnance**[3], **M. A. M. Maqueda**[3], **and Y. Aksenov**[4]

[1]School of Marine Science and Engineering, University of Plymouth, Plymouth, PL4 8AA, UK
[2]Shirshov Institute of Oceanology, 36 Nahimovski prospect, Moscow, 117997, Russia
[3]National Oceanography Centre, Joseph Proudman Building, 6 Brownlow Street, Liverpool, L3 5DA, UK
[4]National Oceanography Centre, European Way, Southampton, SO14 3ZH, UK

Correspondence to: F. Wobus (fred.wobus@plymouth.ac.uk)

Abstract. We investigate the flow of brine-enriched shelf water from Storfjorden (Svalbard) into Fram Strait and onto the western Svalbard Shelf using a regional set-up of NEMO-SHELF, a 3-D numerical ocean circulation model. The model is set up with realistic bathymetry, atmospheric forcing, open boundary conditions and tides. The model has 3 km horizontal resolution and 50 vertical levels in the s_h-coordinate system which is specially designed to resolve bottom boundary layer processes. In a series of modelling experiments we focus on the influence of tides on the propagation of the dense water plume by comparing results from tidal and non-tidal model runs.

Comparisons of non-tidal to tidal simulations reveal a hotspot of tidally induced horizontal diffusion leading to the lateral dispersion of the plume at the southernmost headland of Spitsbergen which is in close proximity to the plume path. As a result the lighter fractions in the diluted upper layer of the plume are drawn into the shallow coastal current that carries Storfjorden water onto the western Svalbard Shelf, while the dense bottom layer continues to sink down the slope. This bifurcation of the plume into a diluted shelf branch and a dense downslope branch is enhanced by tidally induced shear dispersion at the headland. Tidal effects at the headland are shown to cause a net reduction in the downslope flux of Storfjorden water into the deep Fram Strait. This finding contrasts previous results from observations of a dense plume on a different shelf without abrupt topography.

1 Introduction

The Storfjorden is a sill fjord in the Svalbard Archipelago, located between 76°30′–78°30′ N and 17°–22° W, where intense sea ice formation and brine rejection lead to the formation of brine-enriched shelf water (BSW) that subsequently spills over the sill, spreads on the shelf and sinks down the continental slope as a dense water plume (Quadfasel et al., 1988; Schauer, 1995). During the winter freezing period, typically from late November to mid-May, the recurring latent-heat polynya in Storfjorden produces 0.06 to 0.07 Sv ($1\,\mathrm{Sv} \equiv 10^6\,\mathrm{m^3\,s^{-1}}$) of BSW (Schauer, 1995; Haarpaintner et al., 2001; Skogseth et al., 2004). Downstream of the sill the plume initially assumes a two-layer structure – a dense homogenised bottom layer and an overlying diffuse layer (Fer et al., 2003). The upper layer mixes with shelf waters and spreads laterally (Fer et al., 2003), while the densest fractions cascade down the continental slope and occasionally reach depths of over 2000 m (Quadfasel et al., 1988; Schauer et al., 2003). The overflow of dense waters from the Storfjorden has been estimated to account for 5 to 10 % of shelf waters delivered to the deep Arctic Ocean (Quadfasel et al., 1988). Arctic coastal polynyas are estimated to produce a total of 0.7–1.2 Sv of dense water over the entire Arctic Ocean (Cavalieri and Martin, 1994).

The localised occurrence and temporal intermittency of cascading generally means that field campaigns record the outcomes of cascading (e.g. Ivanov et al., 2004) while observations of the process remain largely elusive. Numerical models aim to bridge this gap and progress has been made in the modelling of relatively persistent dense water flows, notably the Faroe Bank Channel (see Legg et al., 2009, and references therein). Cascading occurs in the bottom boundary layer where questions of parameterising turbulent mixing and bottom friction continue to pose unresolved challenges

for 3-D models (Lane-Serff, 2009), especially due to the fine resolution required to represent a small-scale process over large shelf areas. Models of the Storfjorden overflow using a two-layer reduced gravity model (Jungclaus et al., 1995), a 3-D regional model with idealised ambient and forcing conditions (Fer and Ådlandsvik, 2008), or a streamtube model with parameterised entrainment (Akimova et al., 2011) have achieved good agreement of the modelled plume with observations (by Quadfasel et al., 1988; Schauer, 1995; Fer et al., 2003; Skogseth et al., 2008, and others) and contributed greatly to our knowledge of the dynamics and interannual variability of the overflow.

In this study we use a high-resolution regional model (NEMO-SHELF) to investigate the effect of tides on the Storfjorden cascade. Detailed studies into tidal effects on dense water flows were scarce until the AnSlope project (Gordon et al., 2004) in the Ross Sea, Antarctica revealed a dense bottom layer of 100–300 m which is many times the Ekman depth (Padman et al., 2009). An analytical model (Ou et al., 2009) and subsequent numerical experiments (Guan et al., 2009) showed that tidal mixing on the wide and flat Antarctic shelf increases the off-shelf transport of dense shelf waters into the deep basin.

With regards to modelling Arctic Ocean circulation and ocean–ice interactions there is growing understanding that tidal effects should not be neglected (e.g. Holloway and Proshutinsky, 2007; Postlethwaite et al., 2011). In the shallow polynya area of the Storfjorden, where the dense waters are formed, the circulation has been shown to be sensitive to mixing due to wind and tides (Skogseth et al., 2007), but considering Svalbard's complex topography it remains an open question whether the plume's downstream response to tidal forcing is comparable to the findings of Padman et al. (2009) and Ou et al. (2009) in Antarctica. The present study therefore addresses the following questions.

- How do tides affect the Storfjorden overflow plume?
- Which physical processes explain tidally induced modifications in the plume's behaviour?
- Do tides cause an increase in the downslope transport of Storfjorden water into the deep Fram Strait?

The paper is organised as follows: in Sect. 2 we describe the set-up of the numerical model. From a series of experiments that focus on the effects of the tides on the overflow plume we show representative results in Sect. 3. We discuss the physical processes affecting the plume's descent under tidal conditions in Sect. 4, and conclude in Sect. 5 with answers to the above questions.

2 Model description and set-up

2.1 Model domain and resolution

We use a 3-D ocean circulation model, based on NEMO-Shelf (O'Dea et al., 2012), in a regional set-up with realistic bathymetry, atmospheric forcing, open boundary conditions and tides. The 480 km by 540 km domain with a uniform horizontal resolution of 3 km has its south-western corner at 75.0° N, 6.0° E and encompasses most of the Svalbard Archipelago as well as the Storfjordrenna to its south, the Spitsbergen continental slope to its west and parts of the eastern Fram Strait (Fig. 1).

The model bathymetry from IBCAOv3 (Jakobsson et al., 2012) was first interpolated onto the model grid and then slightly adjusted as follows. First, the bathymetry was slightly smoothed using 2-D convolution with a 3×3 Gaussian kernel in order to reduce near-bottom pressure gradient errors. Second, the adjustment of Martinho and Batteen (2006) was applied with a critical slope parameter value of 0.3 which limits slope angles to no more than $\approx 4°$ on the continental slope. This type of bathymetry adjustment, common to σ-level models, preserves numerical stability while remaining faithful to the topographical characteristics of the terrain.

In the vertical we use 50 computational levels in the s_{h}-coordinate system (Wobus et al., 2013) which was especially designed for the modelling of near-bottom density currents. The bottom-most 16 levels follow the terrain such that vertical resolution near the bottom is never coarser than 7.5 m. Equidistant level spacing within the bottom boundary layer avoids any loss in vertical resolution with increasing depth (as is the case with the traditional s-coordinate stretching function). Above the bottom layer three s_{h} levels are inserted at 200, 500 and 1000 m to keep levels in the interior mostly horizontal. This approach follows concepts introduced by Enriquez et al. (2005) and Ivanov (2011).

2.2 Model numerics

The main differences of NEMO-Shelf to the standard NEMO model of Madec (2008) are detailed in O'Dea et al. (2012) and our additional modifications have been described in Wobus et al. (2013). Therefore only a brief summary of the specific code configuration for this study is given here. We use the no-slip bottom boundary implemented by Wobus et al. (2013) in order to explicitly resolve bottom friction and thus better represent the Ekman physics in the bottom boundary layer. The generic length scale (GLS) turbulence model (Umlauf and Burchard, 2003) is used in its k-ϵ configuration (with parameters following Warner et al., 2005) for estimation of vertical diffusivity and viscosity coefficients. This scheme was shown by Ilıcak et al. (2008) to perform satisfactorily when applied to the modelling of overflows. For horizontal eddy diffusivity and viscosity we use a rotated

Laplacian operator oriented along iso-neutral surfaces. Horizontal viscosity coefficients are constant at $20\,m^2\,s^{-1}$ while the horizontal diffusivity coefficients evolve with the flow field according to a Smagorinsky (1963) scheme implemented in NEMO by Luneva and Holt (2010) and further refined in Shapiro et al. (2012).

The two-dimensional Smagorinsky (1963) algorithm was designed to improve the representation of subgrid-scale horizontal diffusion in oceanic and atmospheric circulation models. It assumes that eddy viscosities for horizontal turbulent mixing are proportional to the horizontal deformation of the flow. Such a non-linear scheme is thus a more physically based formulation of horizontal mixing (compared to linear schemes) and has become the preferred method in modern grid-point models (Becker and Burkhardt, 2007).

In NEMO, the Smagorinsky-like small-scale horizontal physics in the conservation equation for tracers – the horizontal diffusion term D_{hor} for heat, salt and passive tracers – is written as (Madec, 2008)

$$D_{\mathrm{hor}} = \nabla \cdot (\kappa_{\mathrm{hor}}\, \Re\, \nabla T)\,, \quad (1)$$

where $\Re$ is a rotation matrix containing the slopes r between the surface along which the diffusive operator acts (in our case $r = \frac{\mathrm{d}\rho}{\mathrm{d}x} / \frac{\mathrm{d}\rho}{\mathrm{d}z}$ for iso-neutral surfaces where ρ is the density, and x and z are horizontal and vertical coordinates respectively) and the model s-level. The horizontal diffusion thus depends on two factors – (i) the horizontal diffusivity coefficient κ_{hor}, which in turn depends on the velocity field (the horizontal tension and the horizontal shearing strain) and (ii) the local tracer gradient ∇T (where T is temperature, salinity or passive tracer concentration). By accounting for the deformation of the flow, the Smagorinsky scheme effectively parameterises lateral shear dispersion arising from current shear and vertical diffusion (Taylor, 1953). In tidal waters particularly, an oscillatory flow over the seabed generates vertical shear, which results in turbulence that is strained by velocity shear leading to an increase in horizontal diffusion and subsequent shear dispersion (Geyer and Signell, 1992; Holt and Proctor, 2001). The efficiency of the Smagorinsky scheme to accurately represent subgrid-scale horizontal diffusion in an s-coordinate NEMO model is evaluated in Shapiro et al. (2012) to which the reader is referred for more details on the algorithm.

2.3 Boundary and initial conditions

The model is initialised with fields taken from a global NEMO simulation using the tripolar ORCA $1/12°$ grid (resolution ca. 3.5 km in the Arctic Ocean, ca. 4 km in the vicinity of Svalbard and ca. 9 km globally) and 75 vertical z levels (the global NEMO is described in detail, e.g. by Blaker et al., 2012). The same model data, provided every 5 days, is also used to force the model's open boundaries. Temperature and salinity are applied using the flow relaxation scheme (FRS) over a 7-grid cell wide FRS zone, while sea surface elevation and barotropic velocities are applied using the Flather condition (Flather, 1976). Each model experiment is run from the end of August 1985 to the end of August 1986, with initial and boundary conditions taken from the global NEMO model data for this period. These times were chosen to coincide with the dense water cascading event described in Quadfasel et al. (1988).

2.4 Atmospheric and tidal forcing

Fields from the Drakkar forcing set (DFS4.1[1]) are applied using the bulk CORE formulation (Large and Yeager, 2004) to calculate atmospheric fluxes at the ocean surface. DFS4.1 was compiled from NCEP and ECMWF reanalysis products by the Drakkar group (Brodeau et al., 2010) and provides global coverage at 320×161 resolution for air temperature and specific humidity at 2 m, wind velocity at 10 m and 192×94 for short and longwave radiation, precipitation and snow. The forcing period matches the 1985–1986 time period of the boundary forcing from the "outer" model.

For tidal model runs we prescribe (again, using the Flather (1976) condition) tidal sea surface elevation and barotropic velocity at the model boundaries, as the "outer" $1/12°$ NEMO model does not include tides. The amplitudes and phases for the Q1, O1, P1, K1, N2, M2, S2, K2 and M4 constituents are extracted from the TPXO7.2 tidal model developed by Egbert and Erofeeva (2002) at Oregon State University. TPXO7.2 is a medium-resolution $0.25° \times 0.25°$ global assimilation model. The tidal model assimilates T/P altimetry between 66° N and S latitudes, ERS (European Remote sensing Satellite) data and coastal and benthic tide gauge data from the Arctic and Antarctic, making it particularly suitable for this study.

Tidal forcing at the domain boundaries is sufficient for our regional model of limited extent compared to tidal potential forcing throughout the domain, which can be useful for very large domains. The performance of the tidal forcing is evaluated by comparison to observations in Sect. 3.2.

2.5 Overflow parameterisation and passive tracers

For the purposes of this study we set up our model to accurately represent, as closely as possible, the downstream evolution of the dense water plume once it has left the fjord. We do not attempt to model the polynya dynamics, sea ice formation, brine rejection and vertical convection that result in the formation and accumulation of dense water in the fjord's interior. A very simple sea ice model is used to block sea surface fluxes where SST (sea surface temperature) drops below freezing temperature to prevent further cooling, but brine rejection is not explicitly represented. Instead we parameterise the outflow based on previous observations in the fjord (Anderson et al., 1988; Schauer, 1995; Haarpaintner, 1999;

[1]Obtained from the National Oceanography Centre's ORCA1 project website at ftp://ftp.noc.soton.ac.uk/omfftp/DFS4.1

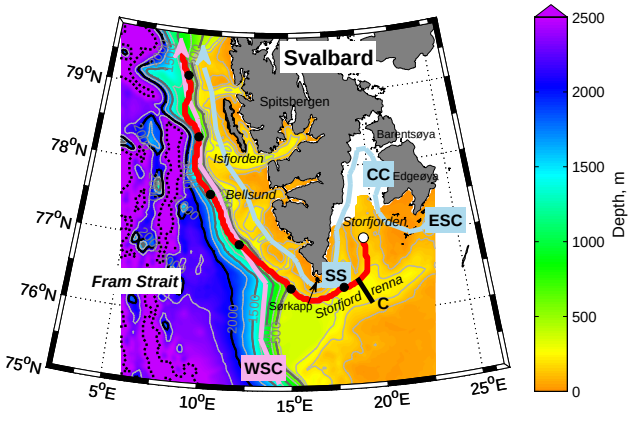

Fig. 1. Bathymetry of the model domain (shaded). Faint contours are drawn every 100 m for the first 400 m, then every 250 m with stronger lines at 500, 1000, 1500 and 2000 m (labelled). The capped bathymetry at 2500 m is shown as a black dotted line. A generalised plume pathway (red line) is marked every 100 km (filled circles) downstream of the sill (open circle). Schematic locations of main currents (taken from Saloranta, 2001; and Skøgseth et al., 2005b) are abbreviated as WSC, West Spitsbergen Current; ESC, East Spitsbergen Current; CC, Cyclonic Coastal Current; and SS, Sørkappstrømmen. Cross-section C (taken in August 2002 by Fer et al., 2004) is shown as a bold line.

Haarpaintner et al., 2001; Fer et al., 2003; Skogseth et al., 2005b, 2008) and the results of dedicated modelling studies (Haarpaintner et al., 2001; Skogseth et al., 2004, 2005a). Our overflow parameterisation is designed to capture the end result of the aforementioned processes inside the fjord.

The inner fjord is excluded from our model by land-masking the basin north of the line between the Crollbreen Glacier (77.2° N, 17.4° E) in the east and Kvalpynten[2] (77.45° N, 20.9° E) in the west (unshaded areas west of Barentsøya and Edgeøya in Fig. 1).

Of the fjord's basin remains a 35 km wide (between 18.9 and 20.3° E) artificial bay behind the sill (located at 77.35° N, 19.5° E) where the injection of water at $T = -1.92\,^{\circ}\mathrm{C}$ with an elevated salinity simulates the end result of the dense water formation processes inside the fjord.

The freezing period and thus dense water accumulation within the fjord starts around November. Beginning between January and March the dense water starts to spill over the sill in a series of pulses (Schauer, 1995) producing an average of 0.06–0.07 Sv of dense water over an overflow period lasting 5–6 months (see Skogseth et al., 2004, 2005a, 2008, for more details). As in Fer and Ådlandsvik (2008), we use an idealised flow rate profile (identical in all runs) to capture the observed variability during an overflow season.

The model is initially run for 140 days from the end of August to mid-January to allow dense water remaining from the previous overflow period (contained in the initial conditions) to drain from the fjord. The prescribed overflow begins in mid-January with a 2 week ramp-up reaching 0.086 Sv by beginning of February, continues at full strength for 60 days until the end of March and ramps back down to zero over 75 days until mid-June. During this period an average of 0.06 Sv exits the injection bay. Each model run continues thereafter for 2.5 months until the end of August giving a total model period of 1 yr per run.

To study the plume's downstream evolution the dense water is marked with online fully diffusive passive tracers. Passive tracers enable a truly Lagrangian view of waters originating in the fjord, something that is near impossible in the ocean where the plume is typically identified by its T-S signature only. We use NEMO's TOP/MYTRC module and additionally implement the lateral boundary condition $\mathrm{d}C/\mathrm{d}x = 0$ to prevent tracer with concentration C from reflecting back into the model domain. We use three passive tracers TRC1, TRC2 and TRC3 (with values 0–1.0) corresponding with the ramp-up, constant flow and ramp-down periods of the overflow cycle to separate the effects of dense water leaving the fjord at different times. A combined picture of the entire plume emerges by simply adding up the three tracer fields.

3 Results

3.1 Experimental set-up

We independently test the response of the dense water plume to overflow strength (i.e. salinity if dense water injected behind the sill), tides (by turning tidal forcing on and off at the model boundaries) and wind strength (by activating the DFS4.1 wind fields or setting them to zero). In total we carry out 16 model runs. Four different overflow scenarios are tested – LOW, MEDIUM, HIGH and EXTREME – with a dense water salinity at the sill of $S_{\mathrm{sill}} = 35.2$, 35.5, 35.8 and 36.1, respectively. While salinities of up to 35.8 have been observed in Storfjorden (Rudels et al., 2005), our most saline scenario ($S_{\mathrm{sill}} = 36.1$) has not been observed and thus represents an idealised extreme end of the parameter space. Each overflow scenario is performed with and without tides, but with atmospheric forcing including winds. Each of these experiments is then repeated without wind. In the following we mainly focus on the results from the HIGH overflow scenario ($S_{\mathrm{sill}} = 35.8$) by comparing the tidal run to its non-tidal control. We refer to zero wind experiments only when it is appropriate to isolate the tidal mixing from wind-driven mixing.

3.2 Comparison with observations – tides

The tidal boundary conditions extracted from the TPOX7.2 tidal model cannot be directly validated because there are no tide gauge observations at those mid-ocean locations

[2] http://stadnamn.npolar.no/ is a useful resource on Svalbard place names.

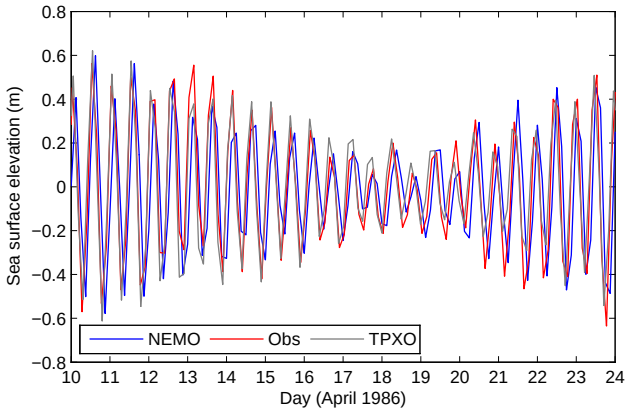

Fig. 2. Comparison of tidal sea level elevation at Ny-Ålesund (approximately 78.95° N, 11.95° E). Data sets shown: NEMO model (blue), UHSLC tide gauge 823A (red) and TPXO7.2 tidal model (grey). Note that the vertical axes of the original data sets have been shifted to a uniform reference height.

coinciding with our domain boundaries. However, a time series of tide gauge readings is available for the location of Ny-Ålesund at approximately 78.95° N, 11.95° E from station 823A of the Joint Archive for Sea Level (JASL)[3]. For the same location a time series of predicted tidal sea surface elevations was extracted from the TPXO7.2 tidal model.

The observed and predicted data sets were averaged into 3-hourly bins to match the frequency of NEMO output. The sea surface elevations for a 2 week semi-diurnal tidal cycle during April 1986 are shown in Fig. 2. The standard deviation of the differences in high/low tide elevations [4] between the modelled (blue) and the observed tides (red) is 0.15 m, while the standard deviation for the TPXO7.2 predictions (grey line) is 0.10 m. We therefore conclude that the NEMO model is able to reproduce tides with approximately the same degree of accuracy as TPXO7.2 which is considered the best available tidal model that also includes data assimilation (which is lacking in our model and therefore a lower accuracy is expected).

The tidal excursion distance was calculated for a 250 m deep location south of Sørkapp at 76.21° N, 16.49° E which lies directly in the path of the plume. Using tidal harmonic analysis (Pawlowicz et al., 2002) of the modelled surface currents we get the excursion distances ($E = 2\,U_{\max}\,T/\pi$, where U is the maximum velocity amplitude of a given tidal constituent and T is its period) of 5.4 km for the M_2 tide and 7.4 km for the K_1 tide.

[3]The data was obtained from http://ilikai.soest.hawaii.edu/uhslc/htmld/d0823A.html.

[4]By using only the high/low tide elevations to compute the standard deviation we effectively eliminate a possible phase shift from this calculation, as it does not effect the resulting velocities.

3.3 Comparison with observations – plume

The overflow strength of our HIGH scenario aims to be representative of deep cascading events that took place in 1986, 1988 and 2002 when a dense water plume of Storfjorden origin was detected deeper than 2000 m in the eastern Fram Strait (Quadfasel et al., 1988; Schauer et al., 2003; Akimova et al., 2011). Large-scale observations in the Storfjorden region were conducted in August 2002 by Fer et al. (2004). Their section C in Storfjordrenna (see location in Fig. 1) is reproduced in Fig. 3 for comparison with our model results.

The observations by Fer et al. (2004) were made in August, approximately 4 months after the overflow peaked around April 2002 (Rudels et al., 2005), while our idealised injection profile achieves peak overflow conditions in March. Figure 3 therefore presents our model results for July in order to compare plumes during the same stage of the flow. The semi-idealised model used in this sensitivity study is not expected to show exact agreement with the conditions in a particular year but rather to capture the major plume characteristics, especially as the overflow is prescribed by injection of dense water based on general parameters.

Comparison of the temperature sections in Fig. 3a and b shows reasonable agreement in the surface temperature, and the depth of the 5.5 °C isotherm is at $\approx$ 30 m in both observed and modelled cross sections. The observed bottom temperature of -1.5 °C is colder compared to 0 °C in the model. This can be explained by observations capturing the remains of the previous year's cascade which aren't present in the initial conditions of our model. The weaker stratification in the model shown in salinity and density sections (Fig. 3c, d and e, f for observed and model data respectively) is attributed to the same difference in ambient conditions at the start of the overflow. Another reason for the rather poor agreement in the salinity of the surface layer is possibly due to the lack of a sophisticated sea ice model (meaning summer ice melt conditions and subsequent freshening aren't reproduced in our model). Such disagreements in the surface layer are, however, deemed acceptable for our study as the surface conditions will not strongly influence the propagation of the plume in the bottom layer, which is the focus of this study. The salinity sections (Fig. 3c, d) show the saline bottom layer of the plume and an overlying fresher layer. A comparable patch of low salinity was noted by Piechura (1996) and further investigated by Fer et al. (2003), who suggested as a possible reason the lateral exchange of fresher shelf water into a layer between the dense plume core and the overlying Atlantic water. The comparison of bottom layer density (Fig. 3e, f) shows good agreement in the slope of isopycnals which "lean" against the Spitsbergen side of the Storfjordrenna (left-hand side of the plots).

We now turn to the modelled spread of Storfjorden Overflow Water (SFOW), which is marked with passive tracers at the point of injection behind the sill. Figure 4 shows the bottom-level concentration of passive tracer in simulations

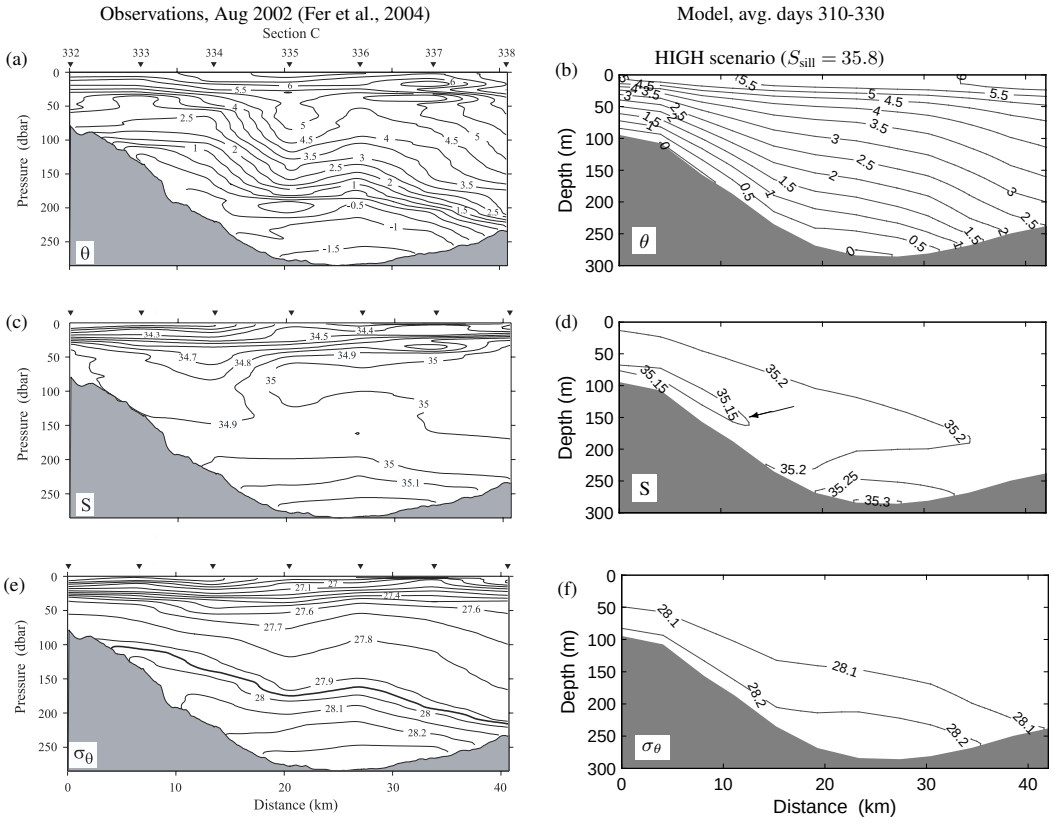

Fig. 3. Comparison of cross section C in Fer et al. (2004) (left) with model of the HIGH overflow scenario ($S_{\text{sill}} = 35.8$, with tides and wind) (right). Observations and averaged model cross sections show the plume approximately 4 months after the peak overflow period. The arrow in **(d)** points out a patch of low salinity.

with and without tides. At the end of each model run – 7.5 months after the start of the overflow – large amounts of dense water have spread out of the fjord and on to the continental slope west of Svalbard, while some overflow tracer still remains "trapped" behind the sill. South of the sill the flow forms eddies and fills the depressions in the Storfjordrenna. This deep channel between the fjord's mouth and Sørkapp steers the plume (assisted by geostrophic adjustment, Fer et al., 2003) west towards the shelf break.

In our model the SFOW first reaches depths greater than 2000 m during early summer and significant amounts of plume water remain at this depth in August (Fig. 4). At this time the plume extent for the HIGH scenario compares well with the locations where in 1986, 1988 and 2002 dense shelf water was observed near the seabed (see Fig. 4b for station locations from Akimova et al., 2011). Our model is thus seen to represent adequately the Ekman advection that facilitates downslope transport of tracer in the bottom boundary layer.

Field observations typically report a bottom layer thickness of 50–60 m, but the plume can be as thin as 10–20 m in the deep Fram Strait (Quadfasel et al., 1988; Schauer, 1995; Schauer and Fahrbach, 1999). In the absence of tracer analysis this is likely an underestimate as the density structure does not show low source water concentrations in the interfacial layer between the plume core and the ambient water. In this study (as in Fer and Ådlandsvik, 2008) the plume thickness is evaluated by passive tracers (using a threshold value of $C_{\text{TRC}} = 0.01$), which is considered to result in an overestimate. A plume thickness on the order of 50–100 m on the shelf (see Fig. 5) is thus seen as a good agreement with observations. However, in the deep Fram Strait at depths > 1000 m our model typically shows a diffuse plume with a thickness in excess of 200–300 m. Previous models by Jungclaus et al. (1995) and Fer and Ådlandsvik (2008) similarly overestimated the thickness of the deep plume. Until better agreement with observations can be achieved in this depth range it appears wise to treat model results in the deep Fram Strait with some caution. In this study we therefore focus on the intermediate part of the flow – from the plume's spread into the Storfjordrenna to the start of its descent down the western Svalbard slope.

3.4 Tidal effects on off-shelf transport

At the end of the modelled overflow period the tracer concentration behind the sill is lower in tidal runs (an example

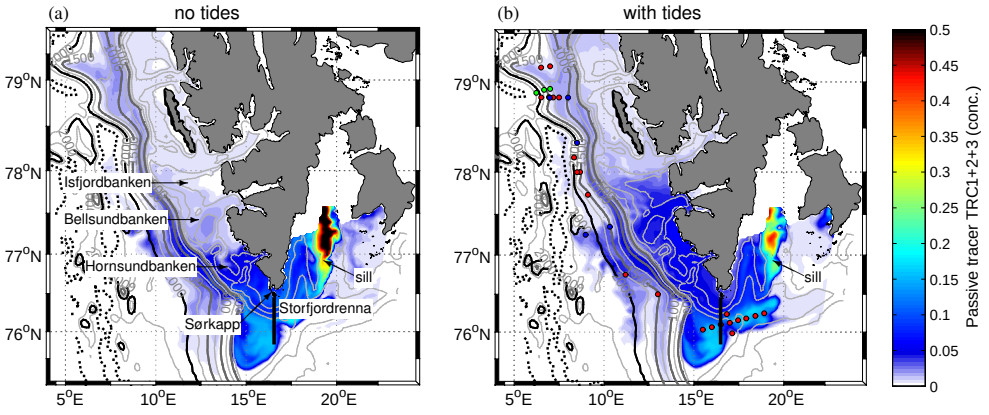

Fig. 4. Snapshot of passive tracer concentration in the bottom model level at the end (31 August) of the model run of the HIGH overflow scenario ($S_{\text{sill}} = 35.8$, with wind). The bold line due south from Sørkapp marks the location of the cross section in Fig. 5. Coloured dots in **(b)** mark CTD stations where the plume was observed in 1986 (blue dots), 1988 (green dots) and 2002 (red dots) (from Akimova et al., 2011).

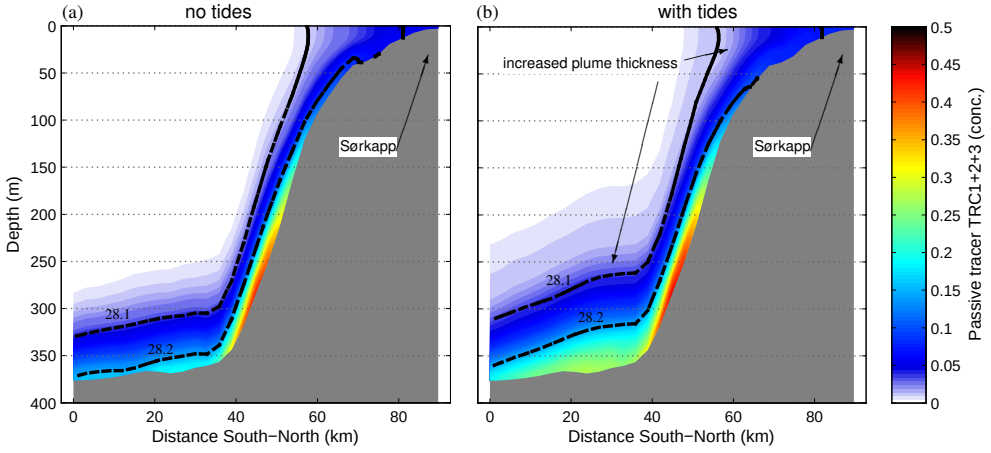

Fig. 5. Cross section of overflow tracer (average concentration during April–May) for a south–north transect from 75.78° N, 16.32° E in Storfjordrenna northwards to the Sørkapp headland at the southern tip of Spitsbergen. The model run is the same as in Fig. 4, the HIGH scenario ($S_{\text{sill}} = 35.8$, with wind), but for a different time of year. The 28.1 and 28.2 km^2 isopycnals (from the same run) are superimposed.

run is shown in Fig. 4b) compared to the non-tidal control run (Fig. 4a). The tides are thus seen to cause a more efficient flushing of dense water from the fjord region towards the shelf edge. Figure 5 compares cross sections of the average tracer concentration during the period of maximum overflow (April–May) at the southern tip of Spitsbergen where the plume leaves the Storfjordrenna. The tidal run (Fig. 5b) reveals a thicker plume of comparable concentration. This, again, suggests increased transport of tracer towards the shelf edge in tidal runs. Increased plume thickness (as shown by tracer concentration) is closely matched by a greater cross-sectional area between sea bed and the isopycnals (overlaid in Fig. 5) to indicate greater potential for downslope transport. The difference in plume thickness caused by tidal effects is not evenly distributed. At a depth of 300–370 m the bottom layer bounded by the 28.2 isopycnal is thicker while in the shallows, between 0 and 100 m depth, the layer between 28.1 and 28.2 kg m^{-3} is thicker. The tidally affected plume is thus denser in the deep part of the trough, but lighter and more diffuse in the shallows.

In the following we compare the fluxes of the model's passive tracer for non-tidal and tidal runs. The tracer flux Q_{TRC} is integrated over the cross-sectional area A from the tracer concentration $C_{\text{TRC}} = \text{TRC}_1 + \text{TRC}_2 + \text{TRC}_3$, where $C_{\text{TRC}} \geq 0.01$ as follows:

$$Q_{\text{TRC}} = \int\int_A C_{\text{TRC}}\,\mathbf{u}\,\mathrm{d}x\,\mathrm{d}z, \tag{2}$$

where $\mathbf{u}$ is the velocity normal to the section in the downstream direction (see arrows in Fig. 6a), and x and z are the horizontal and vertical coordinates respectively. This calculation is carried out for a cross section starting in the deep Fram

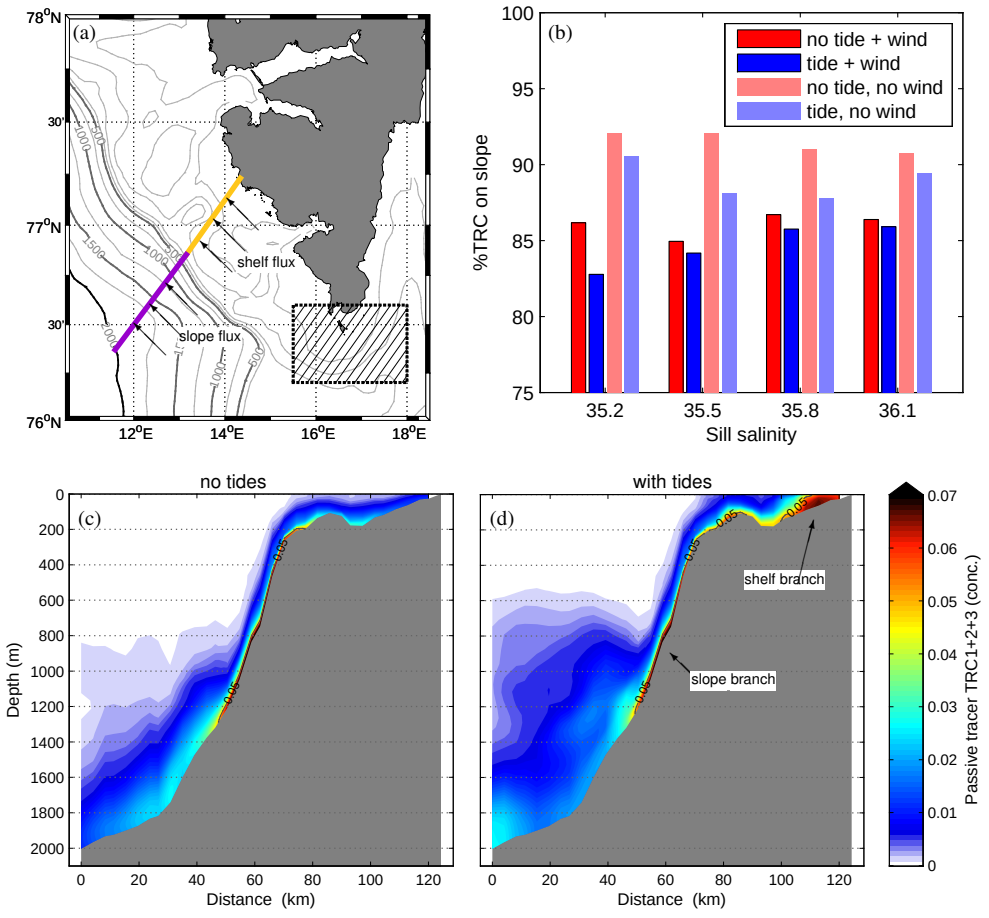

Fig. 6. (a) Location of a cross section divided into *shelf* and *slope* parts for calculation of Q_{TRC} (Eq. 2). The hatched box is the averaging area for Fig. 8. **(b)** percentage of tracer flux passing through the *slope* section out of the total flux measured at the combined slope+self section. Blue bars are tidal runs, red bars are non-tidal runs. Runs with zero wind strength are shown in paler colours for comparison. Panels **(c)** and **(d)** show cross sections of tracer concentration along the transect in **(a)** averaged over the last 2 months (July, August) of the model run (HIGH scenario, with wind). The colour scale was adjusted (compared to previous Figs. 4 and 5) to account for lower tracer concentrations during this stage of the overflow. The isoline of TRC = 0.05 is emphasised.

Strait and reaching onto the western Svalbard Shelf (Fig. 6a). The chosen location is positioned downstream of the shelf in order to test whether tidal effects during the plume's spreading on the shelf cause increased transport into the deep basin. Two parts of the cross section are analysed separately – the *shelf* part in depths of 0–300 m and the *slope* part in depths of 300–2000 m. We then calculate the proportion of the flux through a partial section compared to the total flux passing through the combined section. This method normalises the result and corrects for varying absolute amounts of tracer released in different overflow scenarios.

The relative tracer fluxes through the slope part of the section for all 16 model runs are shown in Fig. 6b. The majority of tracer, 83–92 % of the total, passes through the slope section (at > 300 m depth). It is therefore reasonable to refer to the plume on the slope as the "main" cascade. However, the remainder of 8–17 % of plume waters represents a considerable amount of plume water that does not sink but remains on the shallow shelf.

Figure 6b demonstrates the tides' role in controlling the proportion of plume waters being diverted onto the shelf and thus away from the plume core. In each of the tidal runs a lower proportion of the total tracer flux (a 2 % difference when averaged over all runs) is measured on the slope compared to the shelf. Figure 6c and d, comparing non-tidal with tidal conditions respectively, present cross sections of tracer concentration along the transect shown in Fig. 6a. While the non-tidal plume forms a single branch on the deeper slope (Fig. 6c), the diversion of diluted plume waters onto the shelf under tidal conditions is visible in Fig. 6d where two branches – a deeper slope branch and a shallower shelf branch – are pointed out. The cross sections were plotted from tracer fields averaged over the last two months of the model run (July, August) because closer inspection of plume evolution showed the two-branch structure to develop over

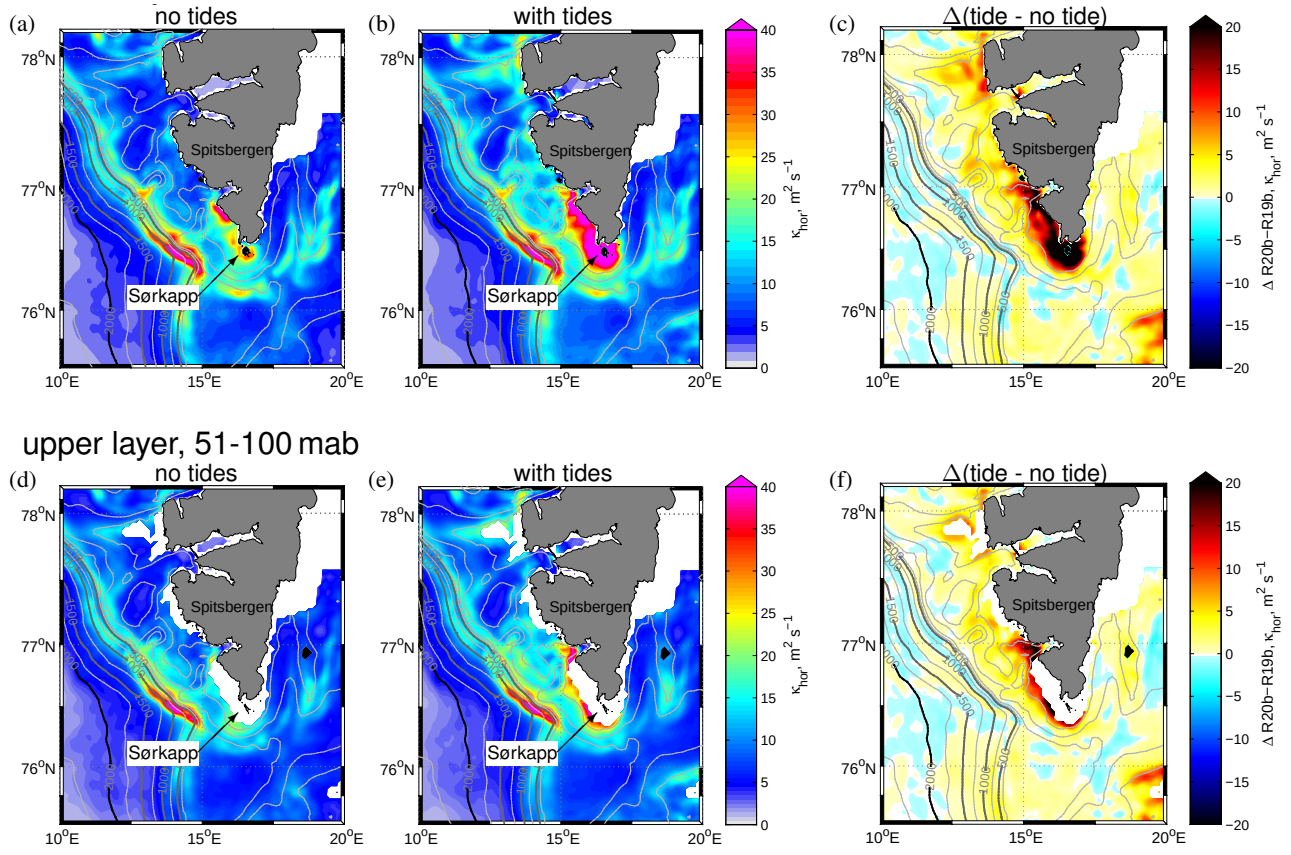

Fig. 7. Horizontal diffusivity coefficient κ_{hor} in the bottom layer (0–50 mab, metres above bottom) **(a–c)** and the upper layer (51–100 mab) **(d–f)**. Values in **(a)**, **(b)** and **(d)**, **(e)** are averaged over the modelled overflow period from mid-January to end of August. The difference is shown in panels **(c)** and **(f)** – warm colours ranging to black represent a tidally induced increase in κ_{hor}.

time, such that the separation of the branches is most evident towards the end of the overflow season.

Qualitatively, the tidally induced dispersion of plume waters onto the shelf is independent of whether wind was included in the model run or not. Wind-driven effects appear to contribute the branching of plume waters onto the shelf as the percentage of slope flux in Fig. 6b is generally lower in model runs with wind compared to those without wind. In the following we focus, however, on tidal effects.

Why is the proportion of plume waters flowing down the deep slope decreased by the tides? To answer this, we backtrack along the plume path and analyse tidal effects on the flow before it splits into shelf and slope branches. The following section will discuss tidal modifications of the plume near the Sørkapp headland, which lies in close proximity to the plume's path during its spreading phase on the shelf.

3.5 Lateral dispersion of the plume

The overflow of tracer in non-tidal and tidal runs starts diverging near the Sørkapp headland. Past this point a smaller proportion of the plume waters sinks down the deeper slope under tidal conditions (Fig. 6b) and tides also cause more overflow water to propagate northwards on the western Svalbard Shelf (Fig. 4). To diagnose the simulated lateral diffusion in the vicinity of Sørkapp, we follow Eq. (1) and analyse variations of the horizontal diffusivity coefficient κ_{hor} and the horizontal tracer gradient ∇T.

The horizontal diffusivity coefficient κ_{hor} is derived from the velocity field by the model's Smagorinsky (1963) scheme. First, we vertically average $\langle\kappa_{\mathrm{hor}}\rangle$ over a 50 m thick bottom layer to capture the horizontal diffusivity governing the densest part of the plume. Then, the process if repeated for the depth layer encountered by the upper layer of the plume at a depth of 51–100 m above bottom. The resulting maps of $\langle\kappa_{\mathrm{hor}}\rangle$ are then averaged over the whole overflow period from mid-January to the end of August to give an impression of its general spatial distribution, which is shown in Fig. 7 for two runs of the HIGH overflow scenario ($S_{\mathrm{sill}} = 35.8$, with wind). The non-tidal vs. tidal comparison reveals that a tidally induced increase in κ_{hor} (up to threefold compared to non-tidal runs) is greatest in the shallow regions around Sørkapp and in other shallow areas where the depth is < 100 m (Fig. 7c). A very similar pattern of tidal increase is evident in the upper layer (Fig. 7f). In fact the tides cause

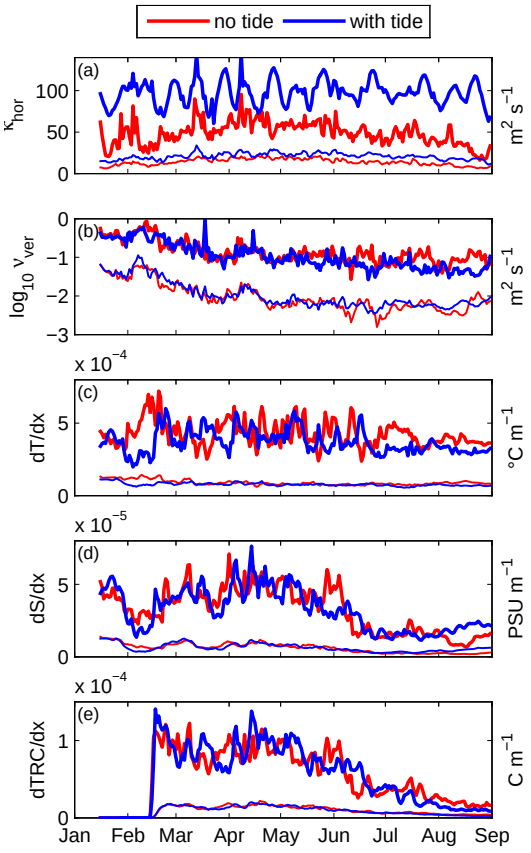

Fig. 8. Time series of averages calculated within a 50 m thick bottom layer over an area around the Sørkapp headland (hatched box in Fig. 6a) for the non-tidal (red) and tidal run (blue) of the HIGH scenario ($S_{sill} = 35.8$, with wind). **(a)** Horizontal diffusivity coefficient, **(b)** vertical viscosity coefficient, **(c)** horizontal temperature gradient, **(d)** horizontal salinity gradient, **(e)** horizontal gradient of passive tracer concentration. Bold lines are maximum values, thin lines are averages.

an increase in κ_{hor} in most areas, with the exception of small patches on the slope showing insignificant change (Fig. 7c, f).

Figure 7c clearly identifies a hotspot of tidally increased diffusion coefficients near Sørkapp. Within a 65 km × 45 km box centred on 76.4° N, 16.8° E (highlighted in Fig. 6a) we calculate spatial averages for a 50 m thick bottom layer of the horizontal diffusivity and vertical viscosity coefficients, as well as several horizontal tracer gradients. The resulting time series plots (Fig. 8) show both maximum and average values for a tidal run (blue) and a non-tidal run (red) of the HIGH overflow scenario.

The time series of κ_{hor} in Fig. 8a emphasises the tidal effect on the horizontal diffusivity coefficient in the Sørkapp region. The maximum as well as average values of κ_{hor} around Sørkapp are consistently higher in the tidal run. The same is true for all other pairs of non-tidal/tidal runs (not shown). The maximum values of the tidal κ_{hor} also reveal a low-frequency signal of biweekly periodicity, which corresponds with spring–neap cycles. In Fig. 8b the vertical viscosity ν_{ver} within the bottom layer is largely the same in the non-tidal and tidal cases, suggesting a weak effect of tides on ν_{ver}.

Similarly we also calculate spatial averages of ∇T in the box around Sørkapp to investigate the tidal influence on the second factor in Eq. (1). The time series of horizontal gradients in temperature, salinity and passive tracer concentration are shown in Fig. 8c–e, respectively. Those time series mostly show no or very little tidal effect on the tracer gradients. Only during July and August there are small differences in the maximum values of tracer gradients at a time when the flow of SFOW near Sørkapp is already diminishing (Fig. 8e).

4 Discussion

In the ocean, the effects of tides cannot be observed in isolation from other processes. To study the effect of tides on the evolution of a dense water plume from its formation in the Storfjorden to its descent into the eastern Fram Strait we set up a regional model of Svalbard. By turning on and off the model's tidal forcing we are able to isolate the tides' contribution to the descent of the Storfjorden overflow plume. Our model uses realistic bathymetry, atmospheric forcing, initial and open boundary conditions, but the details of sea ice formation and polynya dynamics are parameterised rather than represented explicitly by our model. The parameterisation of a the dense water outflow behind the sill is designed to approximate the effects of these processes on the dense water inside the fjord (as described by Haarpaintner et al., 2001; Skogseth et al., 2004, 2005a, and others). Our analysis of the results thus places less emphasis on the upstream plume near the sill and rather focusses on its downstream evolution.

4.1 Tidal augmentation of off-shelf transport

Several mechanisms for tidal effects on the propagation of dense water plumes from the continental shelf towards the shelf edge were suggested by Padman et al. (2009) and supported by an analytical and numerical model (Ou et al., 2009; Guan et al., 2009, respectively). Their studies, based on results of the AnSlope experiment (Gordon et al., 2004), proposed that tidal turbulence increases the plume thickness which lifts the density interface above the Ekman layer where it is shielded from further dilution by frictional processes. Ekman veering within a thicker bottom boundary layer, coupled with tide-induced shear dispersion thus enhances the spread of dense water on the shallow shelf towards the shelf slope (see also Wobus et al., 2011). In addition, the wide, flat shelf in Antarctica inhibits the off-shelf propagation of dense water due to a lack of topographic variation. Tidal effects therefore provide a vital mechanism to explain the observations of a thick and dense water plume on the deeper shelf

slope. In the present case, the channel of the Storfjordrenna provides a mechanism for steering the dense water off the shelf (cf. Fer et al., 2003), even in the absence of tides (see Fig. 4a).

The thickness of a dense plume in steady-state scales with the Ekman depth $D_{\mathrm{Ek}} = \sqrt{2\nu_{\mathrm{ver}}/f\cos\theta}$ (where f is the Coriolis parameter and θ is the slope angle; see Shapiro and Hill, 1997; Wåhlin and Walin, 2001). Our model shows some increase in plume thickness in tidal runs (Fig. 5b), but this cannot be explained by an increase in Ekman depth. In fact, the near-bottom vertical viscosity ν_{ver} in the Sørkapp region is largely unaffected by the tides (Fig. 8b) and the same was found for the vertical diffusivity κ_{ver} (not shown). In our setting, where the plume spreads on a slope, the blurring of the plume interface is attributed to increased horizontal diffusion which is noticeably increased by tidal effects around the headland (see Figs.7c and 8a). On a slope the lateral dispersion of plume tracer is directed upslope. From the shallows where horizontal diffusion is greater due to enhanced tidal effects it continues to spread horizontally thus causing a thicker and more diffuse plume on the deeper slope.

Shear dispersion and the resulting spreading of a tracer in a real flow arise from vertical mixing acting upon a horizontally sheared flow (Taylor, 1953). The lateral spreading of the tracer is not explicitly resolved in our model, but its horizontal diffusion is parameterised by the Smagorinsky (1963) scheme which derives the diffusivity coefficients κ_{hor} from velocity gradients that are explicitly resolved. Tidally enhanced shear alone is the cause for increased κ_{hor} values near the headland where velocities in the shallows reach $1\,\mathrm{m\,s^{-1}}$ during peak tidal flow and thus lead to greater bottom shear. The net result is increased diffusion in Eq. (1), even though the lateral tracer gradient ∇T, remains unaffected by the tides (Fig. 8c, d, e).

4.2 Two-layer structure and bifurcation

The model reveals that, beginning near the Sørkapp headland, the plume effectively forks into two branches separated by the shelf edge. The deep branch that sinks down the slope takes a path that compares well with observations (e.g. Quadfasel et al., 1988; Fer et al., 2003; Akimova et al., 2011). This part of the plume is naturally the denser water from the bottom layer of the plume that incorporates saline remainders from the previous winter (Fer et al., 2003). The lighter fractions of the plume tend to occur in its upper layer and at the lateral edges of the plume. In the shallows, where tidal effects are enhanced, the diluted plume edge is shown to be strongly affected by lateral diffusion (Fig. 7b) which also affects the upper plume layer (Fig. 7e). The widening of the plume towards the shelf not only transports plume waters onto the shelf (Fig. 4b), but must in exchange also import shelf waters into the diluted upper plume layer. This leads to patches of low salinity above the plume core, which were first noted by Piechura (1996) and further investigated by Fer et al. (2003) in sections taken in Storfjordrenna. The latter study showed those fresher waters to have a salinity lower than both the plume core and Atlantic water, which suggests intrusions of fresher shelf waters due to lateral exchanges with the Coastal Current (here called the Sørkappstrømmen (SS), see Fig. 1). This shallow surface current is present in non-tidal as well as tidal runs, but in tidal runs the plume interacts to a greater degree with this current as a result of being lighter (more diluted than in non-tidal runs) and is therefore unable to "dive under" the current which is strongest at the surface. The diluted fractions of plume tracer are thus transported northwards onto the shelf and into the mouths of the Bellsund and Isfjorden (Fig. 4b).

Our model results add to the picture of a two-layer plume by Fer et al. (2003). They showed that the dense bottom layer spreads at a rate consistent with Ekman veering while the diluted upper layer widens at twice the rate as the dense bottom layer. Our tracer analysis shows a shelf-bound pathway of diluted plume waters due to the widening of the plume's lighter fractions into the Coastal Current. We therefore propose that the vertical structure of the plume translates into horizontal bifurcation beginning at the southern headland of Spitsbergen.

Figure 9 develops a schematic of this concept. Figure 9a shows a three-dimensional view of the model output at the end of the same model run as in Fig. 4b (HIGH scenario, with tides and wind). The overlaid arrows highlight the two branches of the plume separated by the edge of the western Svalbard Shelf. A simplified schematic which highlights the two plume layers taking different pathways is shown in Fig. 9b. The low tracer concentrations on the shelf imply that observed temperature and salinity would correspond closely with ambient values and are not representing the plume core. This can explain the lack of observational evidence for the occurrence of SFOW on the western Svalbard Shelf. It may therefore be useful to treat the dispersion of the plume at Sørkapp as a form of "detrainment" of lighter plume waters from its core.

It should further be noted that the depicted vertical separation into two layers is based merely on the qualitative definitions given by Fer et al. (2003) – a dense lower layer with a homogenised density structure and an diffuse upper layer with larger density gradients. For their given observations Fer et al. (2003) additionally defined both layers by fixed density thresholds. Any chosen threshold will depend strongly on the source water characteristics in a given year, and will make it inevitable that the bottom layer will grow thinner through mixing with the overlying layer. The layers in our schematic (Fig. 9b) are therefore merely conceptual, and no general quantitative definition can be given.

The diversion of overflow waters away from the main flow at the headland results in an overall reduction of downslope fluxes into the deep Fram Strait for tidal runs compared to non-tidal simulations. The difference may appear small, but it is nevertheless the opposite of what would be expected

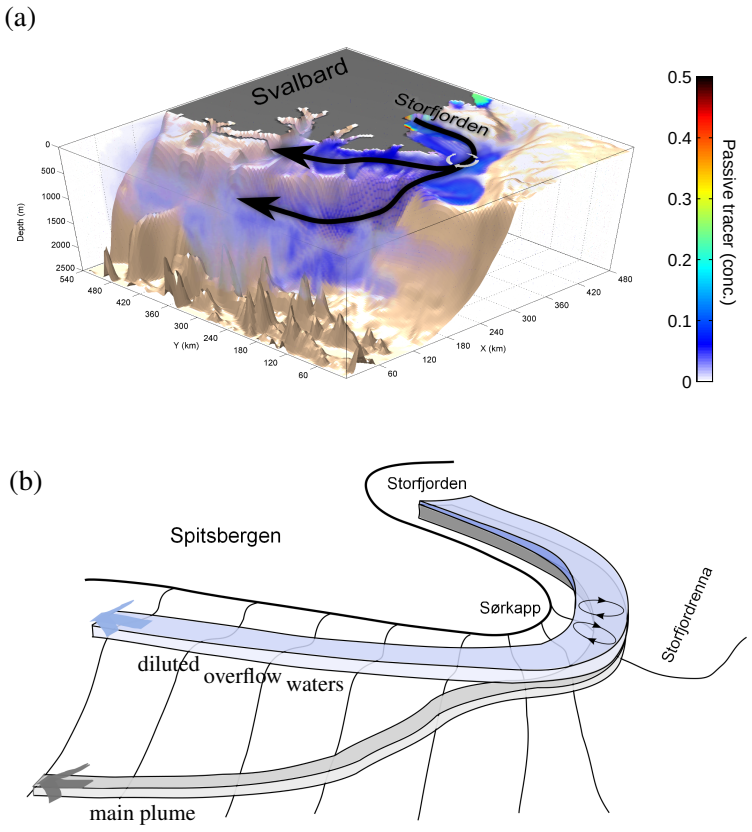

Fig. 9. (a) Three-dimensional volume rendering of tracer concentration for the same day of the tidal run in Fig. 4b (same colour scheme). **(b)** Schematic of tidal dispersion of the Storfjorden overflow plume. Tidally induced shear dispersion near Sørkapp diverts the lighter fractions of plume water from its upper layer onto the shelf.

based on previous findings by Padman et al. (2009), Ou et al. (2009) and Guan et al. (2009), who found that tidal effects increase the downslope transport of dense plumes. Their analysis could assume a wide and flat shelf as the closest headland (Cape Adare) is 65 km from the plume's path. Our study shows a discrepancy with this hypothesis and reveals as its cause the interactions of tides with the complex topography of Svalbard. While it is clear that Storfjorden overflow water does occasionally reach great depths in Fram Strait (Quadfasel et al., 1988; Schauer et al., 2003), we propose that intense overflow events are also coupled with increased transport of fjord water onto the western Svalbard shelf.

5 Summary and conclusions

Using a regional model of Svalbard we are able to gain further understanding of the Storfjorden overflow plume with regards to (i) the AnSlope hypothesis (Padman et al., 2009; Ou et al., 2009; Guan et al., 2009) which elucidates tidal effects on the propagation of dense water plumes, and (ii) the vertical structure of the Storfjorden plume (Fer et al., 2003) and their response to tidal flow. In the upstream section of the flow our model runs including tides confirm a thicker plume and enhanced off-shelf transport of dense water out of the fjord as observed during the AnSlope project. Yet, in contrast to AnSlope results the overall downslope transport of Storfjorden water into the deep Fram Strait is reduced by the tides. We identify the following reasons for the discrepancy.

The plume's path from its formation region in the fjord to the shelf break is intercepted by a headland where tidally enhanced horizontal diffusion results in lateral dispersion of plume waters. The two vertical layers of the plume – a dense bottom layer and a diluted upper layer – are affected by tidal dispersion to different degrees. The widening of the plume and its dilution is enhanced in the upper layer which occupies to a greater degree the shallow coastal side where tidal effects are strongest. The division of the plume into two vertical layers can thus be translated into a bifurcation of the plume path into a deep branch and a shallow branch respectively.

The plume forks into two branches at the southern headland of Spitsbergen, where tidally enhanced lateral exchanges merge the diluted upper plume layer into the shallow Coastal Current that transports lighter fractions of the plume northwards onto the shelf.

In conclusion we propose that the mechanism of tidally induced lateral dispersion of a dense water plume could potentially be significant in other cascading regions where similar topographic features intersect the plume's path between its source and the shelf edge.

Acknowledgements. This work was partly funded by NERC's Core Research Programme Oceans 2025, the EU FP7 MyOcean/MyOcean2 project and a University of Plymouth PhD studentship. We thank Maria Luneva and James Harle (NOCL) for helping to prepare the atmospheric and tidal forcing data. We are also grateful to Ragnheid Skogseth (UNIS) for her instructive comments. Anna Akimova kindly provided the CTD station locations for Fig. 4b. Lastly, we thank four anonymous reviewers for providing helpful insights that greatly improved the manuscript.

Edited by: E. J. M. Delhez

References

Akimova, A., Schauer, U., Danilov, S., and Núñez-Riboni, I.: The role of the deep mixing in the Storfjorden shelf water plume, Deep-Sea Res. Pt. I, 58, 403–414, doi:10.1016/j.dsr.2011.02.001, 2011.

Anderson, L., Jones, E., Lindegren, R., Rudels, B., and Sehlstedt, P.: Nutrient regeneration in cold, high salinity bottom water of the Arctic shelves, Contin. Shelf Res., 8, 1345–1355, 1988.

Becker, E. and Burkhardt, U.: Nonlinear horizontal diffusion for GCMs, Month. Weather Rev., 135, 1439–1454, doi:10.1175/MWR3348.1, 2007.

Blaker, A. T., Hirschi, J. J.-M., Sinha, B., de Cuevas, B., Alderson, S., Coward, A., and Madec, G.: Large near-inertial oscillations of the Atlantic meridional overturning circulation, Ocean Modell., 42, 50–56, doi:10.1016/j.ocemod.2011.11.008, 2012.

Brodeau, L., Barnier, B., Treguier, A.-M., Penduff, T., and Gulev, S.: An ERA40-based atmospheric forcing for global ocean circulation models, Ocean Modell., 31, 88–104, doi:10.1016/j.ocemod.2009.10.005, 2010.

Cavalieri, D. J. and Martin, S.: The contribution of Alaskan, Siberian and Canadian coastal polynyas to the halocline layer of the Arctic Ocean, J. Geophys. Res., 99, 18343–18362, doi:10.1029/94JC01169, 1994.

Egbert, G. and Erofeeva, S.: Efficient inverse modeling of barotropic ocean tides, J. Atmos. Ocean. Technol., 19, 183–204, doi:10.1175/1520-0426(2002)019<0183:EIMOBO>2.0.CO;2, 2002.

Enriquez, C. E., Shapiro, G. I., Souza, A. J., and Zatsepin, A. G.: Hydrodynamic modelling of mesoscale eddies in the Black Sea, Ocean Dyn., 55, 476–489, doi:10.1007/s10236-005-0031-4, 2005.

Fer, I. and Ådlandsvik, B.: Descent and mixing of the overflow plume from Storfjord in Svalbard: an idealized numerical model study, Ocean Science, 4, 115–132, doi:10.5194/os-4-115-2008, 2008.

Fer, I., Skogseth, R., Haugan, P. M., and Jaccard, P.: Observations of the Storfjorden overflow, Deep-Sea Res. Pt. I, 50, 1283–1303, doi:10.1016/S0967-0637(03)00124-9, 2003.

Fer, I., Skogseth, R., and Haugan, P. M.: Mixing of the Storfjorden overflow (Svalbard Archipelago) inferred from density overturns, J. Geophys. Res., 109, C01005, doi:10.1029/2003JC001968, 2004.

Flather, R. A.: A tidal model of the northwest European continental shelf, Memoires de la Societe Royale de Sciences de Liege, 6, 141–164, 1976.

Geyer, W. R. and Signell, R. P.: A reassessment of the role of tidal dispersion in estuaries and bays, Estuar. Coast., 15, 97–108, 1992.

Gordon, A. L., Zambianchi, E., Orsi, A., Visbeck, M., Giulivi, C. F., Whitworth, Thomas, I., and Spezie, G.: Energetic plumes over the western Ross Sea continental slope, Geophys. Res. Lett., 31, L21302, doi:10.1029/2004GL020785, 2004.

Guan, X., Ou, H.-W., and Chen, D.: Tidal effect on the dense water discharge, Part 2: A numerical study, Deep-Sea Res. Pt. II, 56, 884–894, doi:10.1016/j.dsr2.2008.10.028, 2009.

Haarpaintner, J.: The Storfjorden Polynya: ERS-2 SAR observations and overview, Polar Res., 18, 175–182, 1999.

Haarpaintner, J., Gascard, J.-C., and Haugan, P. M.: Ice production and brine formation in Storfjorden, Svalbard, J. Geophys. Res., 106, 14001–14013, doi:10.1029/1999JC000133, 2001.

Holloway, G. and Proshutinsky, A.: Role of tides in Arctic ocean/ice climate, J. Geophys. Res., 112, C04S06, doi:10.1029/2006JC003643, 2007.

Holt, J. T. and Proctor, R.: Dispersion in Shallow Seas, in: Encyclopedia of Ocean Sciences, edited by Steele, J. H., Thorpe, S. A., and Turekian, K. K., 742–747, Elsevier, doi:10.1006/rwos.2001.0348, 2001.

Ilıcak, M., Özgökmen, T. M., Peters, H., Baumert, H. Z., and Iskandarani, M.: Performance of two-equation turbulence closures in three-dimensional simulations of the Red Sea overflow, Ocean Modell., 24, 122–139, doi:10.1016/j.ocemod.2008.06.001, 2008.

Ivanov, V.: How summer ice depletion in the Arctic Ocean may affect the global THC?, Geophys. Res. Abstracts, 13, EGU2011–4457, http://meetingorganizer.copernicus.org/EGU2011/EGU2011-4457.pdf, 2011.

Ivanov, V. V., Shapiro, G. I., Huthnance, J. M., Aleynik, D. L., and Golovin, P. N.: Cascades of dense water around the world ocean, Prog. Oceanogr., 60, 47–98, doi:10.1016/j.pocean.2003.12.002, 2004.

Jakobsson, M., Mayer, L., Coakley, B., Dowdeswell, J. A., Forbes, S., Fridman, B., Hodnesdal, H., Noormets, R., Pedersen, R., Rebesco, M., Schenke, H. W., Zarayskaya, Y., Accettella, D., Armstrong, A., Anderson, R. M., Bienhoff, P., Camerlenghi, A., Church, I., Edwards, M., Gardner, J. V., Hall, J. K., Hell, B., Hestvik, O., Kristoffersen, Y., Marcussen, C., Mohammad, R., Mosher, D., Nghiem, S. V., Pedrosa, M. T., Travaglini, P. G., and Weatherall, P.: The International Bathymetric Chart of the Arctic Ocean (IBCAO) Version 3.0, Geophys. Res. Lett., 39, L12609, doi:10.1029/2012GL052219, 2012.

Jungclaus, J. H., Backhaus, J. O., and Fohrmann, H.: Outflow of dense water from the Storfjord in Svalbard: A numerical model study, J. Geophys. Res., 100, 24719–24728, doi:10.1029/95JC02357, 1995.

Lane-Serff, G. F.: Overflows and Cascades, in: Encyclopedia of Ocean Sciences, edited by John, H. S., Karl, K. T., and Steve, A. T., 265–271, Academic Press, Oxford, 2009.

Large, W. G. and Yeager, S.: Diurnal to decadal global forcing for ocean and sea-ice models : the data sets and flux climatologies. NCAR Technical Note, NCAR/TN-460+STR, Tech. rep., CGD Division of the National Center for Atmospheric Research, 2004.

Legg, S., Chang, Y., Chassignet, E. P., Danabasoglu, G., Ezer, T., Gordon, A. L., Griffies, S., Hallberg, R., Jackson, L., Large, W., Özgökmen, T., Peters, H., Price, J., Riemenschneider, U., Wu, W., Xu, X., and Yang, J.: Improving oceanic overflow representation in climate models: the Gravity Current Entrainment Climate Process Team, Bull. Amer. Meteorol. Soc., 90, 657–670, 2009.

Luneva, M. and Holt, J.: Physical shelf processes operating in the NOCL Arctic Ocean model, Arctic Ocean Model Intercomparison Project, Workshop 14, 19-22 October 2010, Woods Hole Oceanographic Institution, http://www.whoi.edu/fileserver.do?id=77125&pt=2&p=83808, 2010.

Madec, G.: NEMO ocean engine. Note du Pôle de modélisation, Tech. Rep. No. 27, Institut Pierre-Simon Laplace (IPSL), France, http://www.nemoocean.eu/About-NEMO/Reference-manuals, iSSN: 1288-1619, 2008.

Martinho, A. S. and Batteen, M. L.: On reducing the slope parameter in terrain-following numerical ocean models, Ocean Modell., 13, 166–175, doi:10.1016/j.ocemod.2006.01.003, 2006.

O'Dea, E. J., Arnold, A. K., Edwards, K. P., Furner, R., Hyder, P., Martin, M. J., Siddorn, J. R., Storkey, D., While, J., Holt, J. T., and Liu, H.: An operational ocean forecast system incorporating NEMO and SST data assimilation for the tidally driven European North-West shelf, J. Operat. Oceanogr., 5, 3–17, http://www.ingentaconnect.com/content/imarest/joo/2012/00000005/00000001/art00002, 2012.

Ou, H.-W., Guan, X., and Chen, D.: Tidal effect on the dense water discharge, Part 1: Analytical model, Deep-Sea Res. Pt. II, 56, 874–883, doi:10.1016/j.dsr2.2008.10.031, 2009.

Padman, L., Howard, S. L., Orsi, A. H., and Muench, R. D.: Tides of the northwestern Ross Sea and their impact on dense outflows of Antarctic Bottom Water, Deep-Sea Res. Pt. II:, 56, 818–834, 2009.

Pawlowicz, R., Beardsley, B., and Lentz, S.: Classical tidal harmonic analysis including error estimates in MATLAB using T_TIDE, Computers Geosciences, 28, 929–937, doi:10.1016/S0098-3004(02)00013-4, 2002.

Piechura, J.: Dense bottom waters in Storfjord and Storfjordrenna, Oceanologia, 38, 285–292, 1996.

Postlethwaite, C. F., Morales Maqueda, M. A., le Fouest, V., Tattersall, G. R., Holt, J., and Willmott, A. J.: The effect of tides on dense water formation in Arctic shelf seas, Ocean Science, 7, 203–217, doi:10.5194/os-7-203-2011, 2011.

Quadfasel, D., Rudels, B., and Kurz, K.: Outflow of dense water from a Svalbard fjord into the Fram Strait, Deep-Sea Res. Pt. A, 35, 1143–1150, doi:10.1016/0198-0149(88)90006-4, 1988.

Rudels, B., Björk, G., Nilsson, J., Lake, I., and Nohr, C.: The interactions between waters from the Arctic Ocean and the Nordic Seas north of Fram Strait and along the East Greenland Current: results from the Arctic Ocean-02 Oden Expedition, J. Mar. Syst., 55, 1–30, doi:10.1016/j.jmarsys.2004.06.008, 2005.

Schauer, U.: The release of brine-enriched shelf water from Storfjord into the Norwegian Sea, J. Geophys. Res., 100, 16015–16028, doi:10.1029/95JC01184, 1995.

Schauer, U. and Fahrbach, E.: A dense bottom water plume in the western Barents Sea: downstream modification and interannual variability, Deep-Sea Res. Pt. I, 46, 2095–2108, doi:10.1016/S0967-0637(99)00046-1, 1999.

Schauer, U., Rudels, B., Fer, I., Haugan, P. M., Skogseth, R., Björk, G., and Winsor, P.: Return of deep shelf/slope convection in the Western Barents Sea?, in: Seventh Conference on Polar Meteorology and Oceanography and Joint Symposium on High-Latitude Climate Variations, Amer. Meteorol. Soc., Hyannis, MA, 2003.

Shapiro, G. I. and Hill, A. E.: Dynamics of dense water cascades at the shelf edge, J. Phys. Oceanogr., 27, 2381–2394, doi:10.1175/1520-0485(1997)027<2381:DODWCA>2.0.CO;2, 1997.

Shapiro, G., Luneva, M., Pickering, J., and Storkey, D.: The effect of various vertical discretization schemes and horizontal diffusion parameterisation on the performance of a 3-D ocean model: the Black Sea case study, Ocean Science Discuss., 9, 3643–3671, doi:10.5194/osd-9-3643-2012, 2012.

Skogseth, R., Haugan, P. M., and Haarpaintner, J.: Ice and brine production in Storfjorden from four winters of satellite and in situ observations and modeling, J. Geophys. Res., 109, C10008, doi:10.1029/2004JC002384, 2004.

Skogseth, R., Fer, I., and Haugan, P. M.: Dense-water production and overflow from an Arctic coastal polynya in Storfjorden, in: The Nordic Seas: An Integrated Perspective. AGU Geophysical Monograph Series 158, edited by: Drange, H., Dokken, T., Furevik, T., Gerdes, R., and Berger, W., 73–88, Am. Geophys. Union, http://www.agu.org/cgi-bin/agubooks?topic=GM&book=OSGM1584238&search=, 2005a.

Skogseth, R., Haugan, P. M., and Jakobsson, M.: Watermass transformations in Storfjorden, Cont. Shelf Res., 25, 667–695, doi:10.1016/j.csr.2004.10.005, 2005b.

Skogseth, R., Sandvik, A., and Asplin, L.: Wind and tidal forcing on the meso-scale circulation in Storfjorden, Svalbard, Cont. Shelf Res., 27, 208–227, doi:10.1016/j.csr.2006.10.001, 2007.

Skogseth, R., Smedsrud, L. H., Nilsen, F., and Fer, I.: Observations of hydrography and downflow of brine-enriched shelf water in the Storfjorden polynya, Svalbard, J. Geophys. Res., 113, C08049, doi:10.1029/2007JC004452, 2008.

Smagorinsky, J.: General circulation experiments with the primitive equations: I. The basic experiment, Month. Weather Rev., 91, 99–164, 1963.

Taylor, G. I.: Dispersion of Soluble Matter in Solvent Flowing Slowly through a Tube, Proceedings of the Royal Society of London, Series A, Mathemat. Phys. Sci., 219, 186–203, doi:10.1098/rspa.1953.0139, 1953.

Umlauf, L. and Burchard, H.: A generic length-scale equation for geophysical turbulence models, J. Mar. Res., 61, 235–265, doi:10.1357/002224003322005087, 2003.

Wåhlin, A. K. and Walin, G.: Downward migration of dense bottom currents, Environ. Fluid Mechan., 1, 257–279, doi:10.1023/A:1011520432200, 2001.

Warner, J. C., Sherwood, C. R., Arango, H. G., and Signell, R. P.: Performance of four turbulence closure models implemented using a generic length scale method, Ocean Modell., 8, 81–113, doi:10.1016/j.ocemod.2003.12.003, 2005.

Wobus, F., Shapiro, G. I., Maqueda, M. A. M., and Huthnance, J. M.: Numerical simulations of dense water cascading on a steep slope, J. Mar. Res., 69, 391–415, 2011.

Wobus, F., Shapiro, G. I., Huthnance, J. M., and Maqueda, M. A. M.: The piercing of the Atlantic Layer by an Arctic shelf water cascade in an idealised study inspired by the Storfjorden overflow in Svalbard, Ocean Modell., 71, 54–65, 2013.